SIAM J. SCI. COMPUT.
Vol. 34, No. 3, pp. A1544–A1562

INVERSE SOURCE PROBLEMS FOR THE HELMHOLTZ EQUATION AND THE WINDOWED FOURIER TRANSFORM*

ROLAND GRIESMAIER†, MARTIN HANKE†, AND THORSTEN RAASCH†

Abstract. We consider the inverse source problem for time-harmonic acoustic or electromagnetic wave propagation in the two-dimensional free space. Given the radiated far field pattern of the solution to the Helmholtz equation for a certain source term, we find that the windowed Fourier transform of this far field is related to an exponential Radon transform with purely imaginary exponent of a smoothed approximation of the source. Based on this observation we set up a filtered backprojection algorithm to recover information on the unknown source term from a single far field measurement. We analyze this algorithm and provide extensive numerical results that illustrate our theoretical findings. As one outcome the method is shown to work better the larger the wave number. Possible extensions of the reconstruction method to limited aperture data and to inverse obstacle scattering problems are briefly sketched.

Key words. inverse source problem, Helmholtz equation, exponential Radon transform, filtered backprojection

AMS subject classifications. 35R30, 65N21, 44A12

DOI. 10.1137/110855880

1. Introduction.

In this paper we present a new approach for imaging an ensemble of sources for the time-harmonic acoustic wave equation given their radiated far field. With this we stay within the tradition of a considerable number of previous contributions by various authors, including the works [1, 8, 9, 10, 11, 12, 13, 24], to name only those that appear to be most closely connected to our work. Any such approach can also be applied in a straightforward manner to the inverse scattering problem at fixed frequency by treating the scattering obstacle as a source of the scattered wave.

It is well known that the generic acoustic inverse source problem with given far field data at fixed frequency—and presuming the source term f to have compact support—is not uniquely solvable. To ensure uniqueness, additional assumptions are necessary; cf., e.g., Isakov [18] or Ikehata [17]. In a series of recent papers [19, 20, 27], Kusiak and Sylvester therefore introduced a notion of convex scattering support, which is a convex set that is uniquely determined by the given far field, and for which it is known that there exists a source that (i) solves the inverse source problem and (ii) is supported on an arbitrarily small neighborhood of this set; moreover, the convex scattering support is the smallest convex set that has this property. (See section 5 for more details.)

Our new method invokes the windowed Fourier transform of the given far field, which has already been used to estimate the support of source distributions in [2, 3]. We draw a connection of these intermediate data to the exponential Radon transform of the source. The exponential Radon transform differs from the usual Radon transform with respect to the one-dimensional Lebesgue measure ds by an exponential

*Submitted to the journal's Methods and Algorithms for Scientific Computing section November 21, 2011; accepted for publication (in revised form) April 13, 2012; published electronically June 7, 2012.

http://www.siam.org/journals/sisc/34-3/85588.html

†Institut für Mathematik, Johannes Gutenberg-Universität Mainz, 55099 Mainz, Germany (griesmai@uni-mainz.de, hanke@math.uni-mainz.de, raasch@uni-mainz.de).

weight $e^{\mu s}\,\mathrm{d}s$ in the integrand, and in our case the parameter μ is purely imaginary; i.e., $\mu = \mathrm{i}\kappa$, where κ is the wave number. The inversion of this particular instance of the exponential Radon transform is extremely ill-posed; however, in the case of a decent number of point sources one can apply the standard filtered backprojection method from computerized tomography to the modulus of the exponential Radon transform as an imaging technique to achieve a reconstruction with negligible artifacts. If the windowed Fourier transform of the given far field is used as input, this approach yields a blurred representation of the present point sources.

Somewhat surprisingly, the same technique can also be used for the inverse scattering problem: Apparently the resulting image is a reasonable approximation of the convex scattering support and also seems to provide information about the number and relative locations of individual scatterers.

An alternative interpretation of our method arises within the framework of Fourier analysis. It is well known (see (2.3) below) that the given far field is—up to a known factor—the Fourier transform $\widehat{f}$ of the given source, evaluated on the sphere κS^1 of radius κ around the origin. The windowed Fourier transform approach provides a means of extrapolating $\widehat{f}$ to a certain concentric annulus with inner boundary κS^1. The filtered backprojection that we use in the second step of our algorithm is just one option for inverting these Fourier data. It can, in principle, be replaced by any other approximate inverse Fourier transform. Works with related viewpoints from within the area of inverse scattering are, for example, [6, 7, 23].

The plan of the paper is as follows. In the next section we introduce our setting and state the inverse problem to be solved. In sections 3 and 4 we derive the relation between the windowed Fourier transform of the far field data and the exponential Radon transform of an associated source. Then, in section 5 we develop the connection to Fourier inversion and indicate why exponential Radon transform data can be used to approximate the convex scattering support. A more detailed analysis is possible in the special case of point sources to which we turn in section 6. There we outline implementation details of our imaging technique and present numerical results. In section 7 we analyze the resolution of the reconstruction and comment on how to properly sample the far field data, i.e., the input data of the algorithm. In section 8 we comment on possible extensions of the method to limited angle and inverse scattering problems, and finally we conclude with a short summary.

2. Problem setting. For a given distribution with compact support $f \in \mathcal{E}'(\mathbb{R}^2)$ satisfying

$$\operatorname{supp} f \;\subset\; B_R(0) \;:=\; \{\, x \,:\, |x| \le R \}\,, \qquad R > 0\,,$$

we consider the *source problem* for the Helmholtz equation with fixed wave number $\kappa > 0$, that is, find the distributional solution u of the differential equation

$$-\Delta u - \kappa^2 u \;=\; f \qquad \text{in } \mathbb{R}^2 \tag{2.1a}$$

that satisfies the *Sommerfeld radiation condition*

$$\lim_{r\to\infty} \sqrt{r}\left(\frac{\partial u}{\partial r} - \mathrm{i}\kappa u\right) \;=\; 0\,, \qquad r = |x|\,. \tag{2.1b}$$

Recalling the *fundamental solution*

$$\Phi_\kappa(x) \;:=\; \frac{\mathrm{i}}{4}\, H_0^{(1)}(\kappa|x|)$$

of the two-dimensional Helmholtz equation, u can be written as a volume potential

$$u(x) \;=\; (\Phi_\kappa * f)(x) \;=\; \int_{\mathbb{R}^2} \Phi_\kappa(x-z) f(z)\,\mathrm{d}z\,, \qquad x \in \mathbb{R}^2\,, \tag{2.2}$$

with proper interpretation of the convolution, respectively, the integral on the right-hand side. Note that u is smooth away from $\operatorname{supp} f$ (cf., e.g., Dautray and Lions [5, p. 277]) so that the radiation condition makes sense. From (2.2) and the asymptotic behavior of the Hankel functions (cf. Colton and Kress [4, p. 66]) it follows that

$$u(x) \;=\; \frac{e^{\mathrm{i}\pi/4}}{\sqrt{8\pi}}\,\frac{e^{\mathrm{i}\kappa|x|}}{\sqrt{\kappa|x|}}\,u^\infty(\widehat{x}) \;+\; \mathcal{O}(|x|^{-3/2}) \qquad \text{for } |x| \to \infty\,,$$

where $\widehat{x} := x/|x| \in S^1$, and the so-called *far field pattern* u^∞ is given by

$$u^\infty(\widehat{x}) \;=\; \int_{\mathbb{R}^2} e^{-\mathrm{i}\kappa\widehat{x}\cdot z} f(z)\,\mathrm{d}z \;=\; \widehat{f}(\kappa\widehat{x})\,, \qquad \widehat{x} \in S^1\,. \tag{2.3}$$

Here, $\widehat{f}$ denotes the Fourier transform of f. Since f has compact support, the far field belongs to $C^\infty(S^1)$ and $\widehat{f}$ can be extended to an analytic function of its argument $\xi \in \mathbb{C}^2$ (see Hörmander [16, Thm. 7.1.14]). In the following we refer to f as the *source*, u as the *field radiated by* f, and, accordingly, u^∞ as the *far field radiated by* f.

The inverse problem considered in this work is to deduce information on the source f from its radiated far field. We have already mentioned in the introduction that this inverse source problem is not uniquely solvable. For instance, as has been pointed out by several authors, the source

$$f = (\Delta + \kappa^2)v, \qquad v \in C_0^\infty(\mathbb{R}^2),$$

yields the solution $u = -v$ of (2.1) with vanishing far field, and therefore this particular source cannot be detected from far field data. Nonetheless we will outline below a constructive algorithm for visualizing some relevant information about f, or rather, the ensemble of all admissible sources that radiate the same far field. Later, in section 5 we return to the aforementioned nonuniqueness problem.

3. The windowed Fourier transform of the far field pattern. From now on we assume that the given source f is a distribution of order 0; i.e., there exists a constant $C > 0$ such that

$$|f(\phi)| \;\le\; C \sup_{B_R(0)} |\phi| \qquad \text{for all } \phi \in C^\infty(\mathbb{R}^2). \tag{3.1}$$

This means that f can be identified with a bounded linear form on the space of continuous functions of compact support $C_0(\mathbb{R}^2)$ (see, e.g., [16, Thm. 2.1.6]), and accordingly the smallest possible constant C in (3.1) is given by $\|f\|_{C_0'(\mathbb{R}^2)}$, where $\|\cdot\|_{C_0'(\mathbb{R}^2)}$ denotes the norm on the dual space $C_0'(\mathbb{R}^2)$ of $C_0(\mathbb{R}^2)$. By the Riesz representation theorem $C_0'(\mathbb{R}^2)$ can be identified with the space of regular complex Borel measures together with the total variation norm in the sense of measures (see, e.g., Rudin [25, Thm. 6.19]). If $f \in L^1(\mathbb{R}^2)$, then $\|f\|_{C_0'(\mathbb{R}^2)} = \|f\|_{L^1(\mathbb{R}^2)}$.

Note that many interesting source distributions including point sources and single layer potentials meet the assumption (3.1). Others, like double layer potentials, are ruled out by (3.1); it is, however, possible to extend our analysis to more general distributions at the price of somewhat larger error bounds.

Throughout, let $\chi \in \mathscr{S}(\mathbb{R})$ be a smooth even and real *window function* normalized to have integral mean

$$\int_{-\infty}^{\infty} \chi(t)\,\mathrm{d}t \;=\; 1\,, \tag{3.2}$$

and assume its "standard deviation" to be

$$\varepsilon \;:=\; \left(\int_{-\infty}^{\infty} t^2 |\chi(t)|\,\mathrm{d}t\right)^{1/2}. \tag{3.3}$$

(Strictly speaking, the notion of standard deviation requires χ to be nonnegative; nonnegativity of χ, however, is not a necessary requirement in our work.) Then, rewriting $\theta \in S^1$ as $\theta = (\cos\vartheta, \sin\vartheta)$, and likewise setting $\widehat{x}_t = (\cos t, \sin t) \in S^1$ with $\vartheta, t \in \mathbb{R}$, the *windowed Fourier transform* of the far field pattern radiated by f is defined to be

$$\begin{aligned}(Su^\infty)(\theta,\omega) \;&:=\; \int_{-\infty}^{\infty} e^{-\mathrm{i}\omega t}\chi(t) u^\infty(\widehat{x}_{\vartheta+t})\,\mathrm{d}t \\ &=\; \int_{-\infty}^{\infty} e^{-\mathrm{i}\omega t}\chi(t) \int_{\mathbb{R}^2} e^{-\mathrm{i}\kappa \widehat{x}_{\vartheta+t}\cdot z} f(z)\,\mathrm{d}z\;\mathrm{d}t\end{aligned} \tag{3.4}$$

for $\theta \in S^1$ and $\omega \in \mathbb{R}$, where we have made use of (2.3). A short computation shows that

$$e^{-\mathrm{i}\kappa \widehat{x}_{\vartheta+t}\cdot z} = e^{-\mathrm{i}\kappa(\theta+t\theta^\perp)\cdot z} e^{\mathrm{i}\kappa\left((1-\cos t)\theta + (t-\sin t)\theta^\perp\right)\cdot z}, \tag{3.5}$$

where $\theta^\perp := \big(\cos(\vartheta+\pi/2), \sin(\vartheta+\pi/2)\big) = (-\sin\vartheta, \cos\vartheta)$. Introducing

$$E(y,t) \;:=\; e^{\mathrm{i}\left((1-\cos t)\theta + (t-\sin t)\theta^\perp\right)\cdot y} - 1\,, \qquad (y,t) \in \mathbb{R}^2 \times \mathbb{R}\,, \tag{3.6}$$

we can rewrite

$$(Su^\infty)(\theta,\omega) \;=\; \int_{-\infty}^{\infty} e^{-\mathrm{i}\omega t}\chi(t) \int_{\mathbb{R}^2} e^{-\mathrm{i}\kappa(\theta+t\theta^\perp)\cdot z}\big(1 + E(\kappa z, t)\big) f(z)\,\mathrm{d}z\;\mathrm{d}t\,,$$

and, since

$$|\,E(y,t)\,| \;\le\; \frac{1}{2}\,|y|t^2\,, \tag{3.7}$$

we obtain from (3.1) and (3.3) that

$$\begin{aligned}&\left|\int_{-\infty}^{\infty} e^{-\mathrm{i}\omega t}\chi(t) \int_{\mathbb{R}^2} e^{-\mathrm{i}\kappa(\theta+t\theta^\perp)\cdot z} E(\kappa z, t) f(z)\,\mathrm{d}z\;\mathrm{d}t\right| \\ &\qquad\le\; \frac{1}{2}\int_{-\infty}^{\infty} |\chi(t)|\kappa R t^2 \|f\|_{\mathrm{C}_0'(\mathbb{R}^2)}\,\mathrm{d}t \;=\; \frac{1}{2}\,\kappa R\varepsilon^2 \|f\|_{\mathrm{C}_0'(\mathbb{R}^2)}\,.\end{aligned}$$

Thus,

$$\begin{aligned}(Su^\infty)(\theta,\omega) \;&=\; \int_{\mathbb{R}^2} e^{-\mathrm{i}\kappa\theta\cdot z} f(z) \int_{-\infty}^{\infty} \chi(t) e^{-\mathrm{i}t(\kappa\,\theta^\perp\cdot z + \omega)}\,\mathrm{d}t\,\mathrm{d}z \;+\; \mathcal{O}(\kappa R\varepsilon^2\|f\|_{\mathrm{C}_0'(\mathbb{R}^2)}) \\ &=\; \int_{\mathbb{R}^2} f(z) e^{-\mathrm{i}\kappa\theta\cdot z}\widehat{\chi}(\kappa\,\theta^\perp\cdot z + \omega)\,\mathrm{d}z \;+\; \mathcal{O}(\kappa R\varepsilon^2\|f\|_{\mathrm{C}_0'(\mathbb{R}^2)})\,.\end{aligned} \tag{3.8}$$

Note that the first summand on the right-hand side of (3.8) is smooth with respect to θ and ω, which can be seen in the usual way by regularizing f.

Next, we recall the *exponential Radon transform* $T_\mu : C_0^\infty(\mathbb{R}^2) \to C_0^\infty(S^1 \times \mathbb{R})$ with exponent $\mu \in \mathbb{C}$, defined by

$$(T_\mu g)(\phi, s) := \int_{x\cdot\phi=s} e^{\mu x\cdot\phi^\perp} g(x)\,\mathrm{d}x = \int_{-\infty}^{\infty} e^{\mu t} g(s\phi + t\phi^\perp)\,\mathrm{d}t\,; \tag{3.9}$$

cf., e.g., Natterer [21, p. 47]. This transform can be extended to distributions with compact support, i.e., from $\mathcal{E}'(\mathbb{R}^2)$ to $\mathcal{E}'(S^1 \times \mathbb{R})$, by means of its adjoint transform $T_\mu^* : C^\infty(S^1 \times \mathbb{R}) \to C^\infty(\mathbb{R}^2)$,

$$(T_\mu^* h)(x) = \int_{S^1} e^{\overline{\mu} x\cdot\phi^\perp} h(\phi, \phi\cdot x)\,\mathrm{d}\phi$$

(see Helgason [14, p. 32] for the special case $\mu = 0$): Given $g \in \mathcal{E}'(\mathbb{R}^2)$, define $T_\mu g$ via

$$\langle T_\mu g, h\rangle := \langle g, T_\mu^* h\rangle \qquad \text{for all } h \in C^\infty(S^1 \times \mathbb{R})\,. \tag{3.10}$$

Approximating f by a sequence $(f_n)_{n\in\mathbb{N}} \subset C_0^\infty(\mathbb{R}^2)$ (in the sense of distributions) and substituting $z = s\theta^\perp - t\theta$ in (3.8), we find that

$$\begin{aligned}
\int_{\mathbb{R}^2} f_n(z) e^{-\mathrm{i}\kappa\theta\cdot z} \widehat{\chi}(\kappa\,\theta^\perp\cdot z + \omega)\,\mathrm{d}z &= \int_{-\infty}^{\infty} \widehat{\chi}(\kappa s + \omega) \int_{-\infty}^{\infty} e^{\mathrm{i}\kappa t} f_n(s\theta^\perp - t\theta)\,\mathrm{d}t\,\mathrm{d}s \\
&= \int_{-\infty}^{\infty} \widehat{\chi}(\kappa s + \omega)\,\big(T_{\mathrm{i}\kappa} f_n\big)(\theta^\perp, s)\,\mathrm{d}s \\
&= \Big(\psi * \big(T_{\mathrm{i}\kappa} f_n\big)\Big)\Big(\theta^\perp, -\frac{\omega}{\kappa}\Big)\,,
\end{aligned}$$

where the convolution on the right-hand side acts on the second variable only, and ψ is defined via $\psi(s) = \widehat{\chi}(\kappa s)$. Note that χ has been assumed to be real and symmetric. Passing to the limit $n \to \infty$, which is justified by the definition (3.10), we can rewrite the windowed Fourier transform of the far field pattern radiated by f in the following form.

PROPOSITION 3.1. *Let $\chi \in \mathscr{S}(\mathbb{R})$ be real and symmetric with integral mean* 1 *and standard deviation ε as in* (3.2) *and* (3.3)*. Then the windowed Fourier transform with window χ of the far field pattern u^∞ satisfies*

$$(Su^\infty)(\theta,\omega) = \Big(\psi * \big(T_{\mathrm{i}\kappa} f\big)\Big)\Big(\theta^\perp, -\frac{\omega}{\kappa}\Big) + \mathcal{O}\big(\kappa R\varepsilon^2 \|f\|_{\mathrm{C}_0'(\mathbb{R}^2)}\big) \tag{3.11}$$

for $\theta \in S^1$ and $\omega \in \mathbb{R}$, where $\psi(s) = \widehat{\chi}(\kappa s)$. The remainder term in (3.11) *is uniformly bounded by $\frac{1}{2}\kappa R\varepsilon^2 \|f\|_{\mathrm{C}_0'(\mathbb{R}^2)}$.*

Remark 3.2. The pointwise evaluation in the previous formula makes sense, because—as already pointed out after (3.8)—the first term on the right-hand side is smooth. ◇

We mention that the convolution kernel ψ that enters (3.11) satisfies

$$\psi(0) = \widehat{\chi}(0) = \int_{-\infty}^{\infty} \chi(t)\,\mathrm{d}t = 1\,. \tag{3.12}$$

Thus, if we presume (3.2) to be a basic constraint, the magnitude of the first term on the right-hand side of (3.11) is largely independent of the standard deviation ε of

χ, and we can trigger ε appropriately to drive the remainder term in (3.11) small—in a pointwise sense. (This is true, in particular, when f is an ensemble of point sources, as we will later illustrate in more detail in section 6.) Accordingly, when ε is small, then we basically consider the windowed Fourier transform of the far field as a good approximation of an exponential Radon transform of the given source, convolved by the convolution kernel ψ.

4. The exponential Radon transform. Proposition 3.1 suggests a means of reconstructing the source, or of deducing information about the source from the given far field. First, one computes the windowed Fourier transform of the far field, respectively, its rescaled version on the left-hand side of (3.11). Then, by choosing the size ε of the window sufficiently small, one might neglect the remainder term in (3.11), unfold the convolution with ψ, and finally, invert the exponential Radon transform.

However, this approach does not appear to be feasible. First, the deconvolution with ψ is ill-posed and does not even have a unique solution if the Fourier transform of ψ has compact support, which is the generic case in practice, as $\widehat{\psi}(\sigma) = \frac{2\pi}{\kappa}\chi(-\sigma/\kappa)$. Second, although there do exist explicit inversion formulas for the exponential Radon transform (see Tretiak and Metz [28] or [21, p. 48] for real exponents, and You [29] or Natterer [22] for the case of complex exponents), the inversion of the exponential Radon transform with purely imaginary exponents is a severely ill-posed problem (cf., e.g., the discussion in [22]).

We will therefore follow a different approach in what follows. To this end we mention that the exponential Radon transform satisfies a convolution law in its second variable, i.e.,

$$T_\mu(g * f) \;=\; (T_\mu g) * (T_\mu f)\,, \qquad f \in \mathcal{E}'(\mathbb{R}^2)\,,\ g \in \mathscr{S}(\mathbb{R}^2)\,; \tag{4.1}$$

cf. [21, (II.6)]. In [21], μ is assumed real and $f \in \mathscr{S}(\mathbb{R}^2)$; however, for general $\mu \in \mathbb{C}$ the assertion (4.1) can easily be checked by a standard calculation; the generalization to distributions, finally, follows by a regularization argument recalling (3.10). Note that the convolution on the left of (4.1) is in $\mathbb{R}^2$, whereas the convolution on the right acts on the scalar real variable only.

Using the convolution law (4.1) we can change our point of view and reinterpret (3.11) as a means of computing the exponential Radon transform of a smooth mollification $g * f$ of the source, where g is suitably chosen. We provide an example below; see Example 4.2.

PROPOSITION 4.1. *Let $g \in \mathscr{S}(\mathbb{R}^2)$ be real-valued and rotationally symmetric. Then $\big(T_{\mathrm{i}\kappa} g\big)(\theta, \cdot\,)$ is an even real-valued function in $\mathscr{S}(\mathbb{R})$ that does not depend on $\theta \in S^1$, and*

$$\chi(t) := \frac{\kappa}{2\pi}\widehat{\psi}(-\kappa t), \qquad \textit{where} \quad \psi(s) := \big(T_{\mathrm{i}\kappa} g\big)(\theta, s)\,,$$

belongs to $\mathscr{S}(\mathbb{R})$ as well and is real-valued and even. Moreover, $\int \chi \,\mathrm{d}t = 1$ if and only if $\int_0^\infty \cos(\kappa t) g(t\theta)\,\mathrm{d}t = 1/2$. Then the windowed Fourier transform with window χ of the far field pattern u^∞ radiated by f satisfies

$$\big(Su^\infty\big)(\theta, \omega) \;=\; \big(T_{\mathrm{i}\kappa}(g * f)\big)\Big(\theta^\perp, -\frac{\omega}{\kappa}\Big) \;+\; \mathcal{O}\big(\kappa R \varepsilon^2 \|f\|_{\mathrm{C}_0'(\mathbb{R}^2)}\big)\,, \tag{4.2}$$

where ε is as in (3.3).

Proof. We rewrite $g(x) = \varrho(|x|^2)$ for a suitable real-valued function ϱ over the nonnegative real axis which decays faster near infinity than any polynomial grows.

Then

$$\big(T_{\mathrm{i}\kappa} g\big)(\theta, s) \;=\; \int_{-\infty}^{\infty} e^{\mathrm{i}\kappa t}\, \varrho(s^2 + t^2)\, \mathrm{d}t$$

is well defined and independent of θ, and $\psi = \big(T_{\mathrm{i}\kappa} g\big)(\theta, \cdot\,) \in \mathscr{S}(\mathbb{R})$. Furthermore, since ϱ is real-valued,

$$\psi(s) \;=\; 2 \int_0^{\infty} \cos(\kappa t)\, \varrho(s^2 + t^2)\, \mathrm{d}t\,.$$

Hence ψ is real-valued and even, and so is its Fourier transform, and thus χ. Formula (4.2) then follows from (3.11) and (4.1). Finally, as in (3.12), we have that $\psi(0)$ equals the mean of χ over $\mathbb{R}$, which completes the proof. ∎

An important example for Proposition 4.1 is the case when the mollifier g is a Gaussian.

Example 4.2. Let $\varepsilon > 0$ and

$$g_\varepsilon(x) \;:=\; \frac{\varepsilon\kappa}{\sqrt{2\pi}} e^{1/(2\varepsilon^2)} e^{-\frac{1}{2}|x|^2 \varepsilon^2 \kappa^2}\,, \qquad x \in \mathbb{R}^2\,, \tag{4.3}$$

be a rescaled two-dimensional Gaussian with standard deviation $1/(\varepsilon\kappa)$. For $\theta \in S^1$ and $s \in \mathbb{R}$ we compute

$$\begin{aligned}\big(T_{\mathrm{i}\kappa} g_\varepsilon\big)(\theta, s) \;&=\; \int_{-\infty}^{\infty} e^{\mathrm{i}\kappa t} g_\varepsilon(s\theta + t\theta^\perp)\, \mathrm{d}t \;=\; \frac{\varepsilon\kappa}{\sqrt{2\pi}} e^{1/(2\varepsilon^2)} \int_{-\infty}^{\infty} e^{\mathrm{i}\kappa t} e^{-\frac{1}{2}\varepsilon^2\kappa^2(s^2+t^2)}\, \mathrm{d}t \\ &=\; \frac{\varepsilon\kappa}{\sqrt{2\pi}}\, e^{1/(2\varepsilon^2)} e^{-\frac{1}{2}\varepsilon^2\kappa^2 s^2} \int_{-\infty}^{\infty} e^{-\frac{1}{2}\varepsilon^2\kappa^2 t^2 + \mathrm{i}\kappa t}\, \mathrm{d}t\,.\end{aligned}$$

Since the last integral equals $\frac{\sqrt{2\pi}}{\varepsilon\kappa}\, e^{-1/(2\varepsilon^2)}$, we find that

$$\psi_\varepsilon(s) := \big(T_{\mathrm{i}\kappa} g_\varepsilon\big)(\theta, s) \;=\; e^{-\frac{1}{2}\varepsilon^2\kappa^2 s^2}\,, \qquad s \in \mathbb{R}\,, \tag{4.4}$$

i.e., for any $\theta \in S^1$, ψ_ε is a one-dimensional Gaussian with standard deviation $1/(\varepsilon\kappa)$, rescaled by the constant multiplicative factor $\sqrt{2\pi}/(\varepsilon\kappa)$.

Accordingly, the associated window $\chi = \chi_\varepsilon$ of Proposition 4.1 equals

$$\chi_\varepsilon(t) \;=\; \frac{\kappa}{2\pi}\, \widehat{\psi}_\varepsilon(-\kappa t) \;=\; \frac{1}{\sqrt{2\pi}\varepsilon}\, e^{-\frac{1}{2}t^2/\varepsilon^2}\,, \qquad t \in \mathbb{R}\,, \tag{4.5}$$

i.e., χ_ε is a one-dimensional Gaussian window function with standard deviation ε.

The "width" of the (rescaled) Gaussian g_ε is proportional to its standard deviation $1/(\varepsilon\kappa)$; see Figure 4.1 for an illustration. It shows a two-dimensional Gaussian with standard deviation 1: Visually, the dashed line with radius $r_2 = 2$ indicates the extent of the Gaussian, although the values outside of this circle are still significant. At $r_3 = 3$ the values of the Gaussian have dropped down to 1% of the maximum at the center. We adopt a common rule of thumb and, further on, refer to r_3 as the *support radius* of the Gaussian, and to r_2 as its *width*. ◇

In the remainder of this paper we confine ourselves to the Gaussian filter χ_ε of (4.5) for the windowed Fourier transform, which we denote by S_ε in this case, and aim for a mollified approximation $g_\varepsilon * f$ of the source f, where g_ε is the Gaussian mollifier from (4.3).

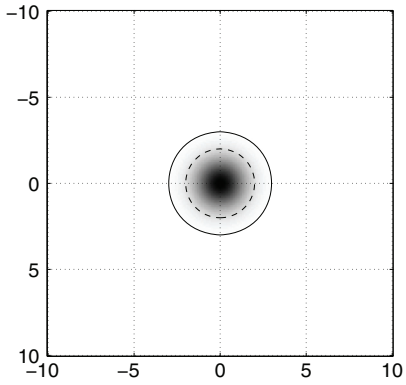

FIG. 4.1. *Gray-scale plot of a two-dimensional Gaussian with standard deviation* 1 *focused at the origin. The dashed line (solid line) corresponds to a circle with radius* $r_2 = 2$ *(*$r_3 = 3$*).*

5. Uniqueness considerations and Fourier inversion. In this section we give a somewhat qualitative interpretation of our analytical findings and also address once again the nonuniqueness issue for the inverse source problem.

Following Sylvester [27], we say that a compact set $\Omega \subset \mathbb{R}^2$ *carries* a far field if every open neighborhood of Ω supports a source that radiates that far field. Accordingly, the *convex source support* $\mathscr{C}$ of a far field u^∞ is defined as the intersection of all compact convex sets $\Omega \subset \mathbb{R}^2$ that carry u^∞. $\mathscr{C}$ is known to be the smallest convex set that carries the given data.

Let f^* be a corresponding source that lives in a small neighborhood of $\mathscr{C}$ and radiates the given far field. By a suitable construction (see [19]) we can choose f^* to be smooth. In what follows we will make the assumption that ε is chosen sufficiently small so that the remainder term in Proposition 4.1 (for that particular source f^*) is negligible.

In this case we conclude from (3.9), (4.2), and Example 4.2 that the windowed Fourier transform of u^∞, with window function χ_ε of (4.5), is essentially zero for every argument (θ, ω) for which the line

$$\Gamma(\theta,\omega) := \left\{ z \in \mathbb{R}^2 \,:\, z = t\theta - \frac{\omega}{\kappa}\,\theta^\perp,\ t \in \mathbb{R} \right\}$$

does not intersect the (convex and compact) $3/(\varepsilon\kappa)$ neighborhood of $\mathscr{C}$. On the other hand, following the argumentation in Hertle [15, Thm. 2.1] (see also Strichartz [26] and [14, Cor. 2.8]), one can establish the following *support theorem* for the exponential Radon transform with complex exponent.

THEOREM 5.1. *Let* $h \in C_0^\infty(\mathbb{R}^2)$ *be such that* $T_\mu h$, $\mu \in \mathbb{C}$, *is zero on every line* Γ *not intersecting a fixed compact convex set* $\mathscr{K}$. *Then* h *is zero outside* $\mathscr{K}$.

Accordingly, up to certain approximation errors, we conclude that we can utilize the windowed Fourier transform $S_\varepsilon u^\infty$ to read off the $3/(\varepsilon\kappa)$ (or even $2/(\varepsilon\kappa)$) neighborhood of $\mathscr{C}$. However, as we will illustrate later numerically (see section 8), we actually obtain even more qualitative information about the location of sources within $\mathscr{C}$.

Another interesting aspect is the connection of our approach to Fourier inversion techniques. According to the Fourier slice theorem for the exponential Radon transform there holds

$$\left(T_{\mathrm{i}\kappa} h\right)^\wedge(\theta,\sigma) = \widehat{h}(\sigma\theta - \kappa\theta^\perp), \qquad \theta \in S^1,\ \sigma \in \mathbb{R}\,, \tag{5.1}$$

where on the left-hand side the Fourier transform acts on the second argument only (see [21, p. 47]). It thus follows from Proposition 4.1 that our data (approximately) determine the Fourier transform of $g_\varepsilon * f^*$ in the exterior of the ball $B_\kappa(0)$.

At the same time, the convolution theorem for the Fourier transform yields

$$\big(g_\varepsilon * f^*\big)^\wedge(\xi) \,=\, \widehat{g}_\varepsilon(\xi)\widehat{f^*}(\xi)\,, \qquad \xi \in \mathbb{R}^2\,, \tag{5.2}$$

where

$$\widehat{g}_\varepsilon(\xi) \,=\, \frac{\sqrt{2\pi}}{\varepsilon\kappa}\, e^{\frac{1}{2}(\kappa^2-|\xi|^2)/(\varepsilon^2\kappa^2)}\,. \tag{5.3}$$

By construction this expression equals $\sqrt{2\pi}\,\widehat{f^*}(\xi)/(\varepsilon\kappa)$ for $|\xi| = \kappa$, while for $|\xi| > \kappa$ the factor in front of $\widehat{f^*}(\xi)$ is essentially zero whenever $(\varepsilon\kappa)\widehat{g}_\varepsilon(\xi)/\sqrt{2\pi}$ is. It follows from (5.3) that this is the case whenever $|\xi|^2 > \kappa^2(1+9\varepsilon^2)$. In other words, the convolution $g_\varepsilon * f^*$ is essentially bandlimited with bandwidth

$$b \,:=\, \kappa\sqrt{1+9\varepsilon^2}\,, \tag{5.4}$$

and thus, the exponential Radon transform with exponent $\mu = \mathrm{i}\kappa$ of $g_\varepsilon * f^*$ provides certain access via (5.1) and (5.2) to the Fourier transform of f^* in the annulus

$$\kappa \,\le\, |\xi| \,\lesssim\, \kappa\sqrt{1+9\varepsilon^2}\,. \tag{5.5}$$

In some sense we may therefore interpret our approach as a nonstandard extrapolation of the Fourier transform of $\widehat{f^*}$ from κS^1 (cf. (2.3)) to the annulus (5.5).

6. Point sources. To motivate our approach of visualizing the source, given the windowed Fourier transform $S_\varepsilon u^\infty$ of its radiated far field, we first consider the case of a single point source; that is, we assume

$$f \,=\, \delta_z \tag{6.1}$$

in (2.1), with δ_z the delta function located in $z \in \mathbb{R}^2$. The exponential Radon transform of this source is given by

$$\big(T_{\mathrm{i}\kappa}\delta_z\big)(\theta,s) \,=\, e^{\mathrm{i}\kappa z\cdot\theta^\perp}\delta(s - z\cdot\theta)\,, \tag{6.2}$$

and its support is the graph of the function

$$\theta \,\mapsto\, s \,=\, z\cdot\theta \,=\, r\cos(\vartheta-\varphi) \tag{6.3}$$

if the source point has the coordinates $z = r(\cos\varphi, \sin\varphi)$; recall that ϑ is the polar angle of $\theta \in S^1$.

For f as in (6.1) the solution u of (2.1) is a shifted fundamental solution,

$$u(x) \,=\, \frac{\mathrm{i}}{4}H_0^{(1)}(\kappa|x-z|)$$

(cf. (2.2)), and, according to (3.11), the windowed Fourier transform of its far field, using a Gaussian filter χ_ε as in (4.5), yields (approximately) a convolution in the s-variable of the graph of $T_{\mathrm{i}\kappa}\delta_z$ of (6.2) with the (rescaled) Gaussian ψ_ε of (4.4), i.e.,

$$\big(S_\varepsilon u^\infty\big)(-\theta^\perp,-s\kappa) \,\approx\, e^{\mathrm{i}\kappa z\cdot\theta^\perp}e^{-\frac{1}{2}\varepsilon^2\kappa^2(s-z\cdot\theta)^2}\,. \tag{6.4}$$

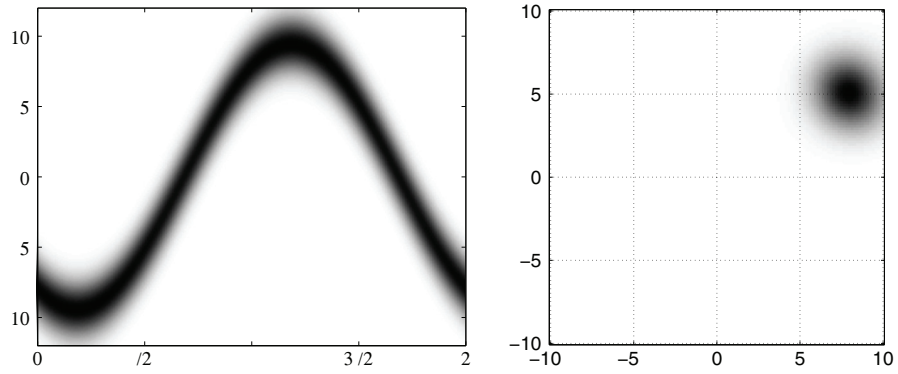

FIG. 6.1. *Left: approximation* (6.5) *of the Radon transform. Right: reconstruction with filtered backprojection.*

Accordingly, a gray-scale plot of the left-hand side of (6.4) looks like a *sine ribbon* of (vertical) diameter $4/(\varepsilon\kappa)$ around the cosine graph (6.3); cf. the left-hand plot of Figure 6.1.

Note that when we turn to the absolute value of the right-hand side of (6.4), this becomes—up to a constant factor—the classical Radon transform $R(g_\varepsilon * \delta_z)$. In other words, the windowed Fourier transform of the far field of a single point source is, up to a phase function and a constant scaling factor, approximately the classical Radon transform of a Gaussian located in that source point, i.e.,

$$\big(R(g_\varepsilon * f)\big)(\theta, s) \;\approx\; \big|\big(S_\varepsilon u^\infty\big)(-\theta^\perp, -s\kappa)\big|\,. \tag{6.5}$$

The support radius of that Gaussian is given by $3/(\varepsilon\kappa)$, its visual width by $2/(\varepsilon\kappa)$. As a consequence, we can compute a mollified approximation $g_\varepsilon * f$ of the point source (6.1) by applying the inverse Radon transform to the right-hand side of (6.5). Below we will also adopt the usual terminology for the Radon transform and call the plot of the absolute values of the windowed Fourier transform a *sinogram*.

If the far field is given at N equidistant points $\theta_j \in S^1$, $j = 1, \ldots, N$, then the data we obtain for (6.5) correspond to a standard Radon data set for the so-called parallel scanning geometry in the plane, where θ takes the values $\theta_1, \ldots, \theta_N \in S^1$, and, for each of these angles, s runs through the same equidistant grid on the real line; see (7.1) below. Accordingly, we can use the classical filtered backprojection algorithm to invert the windowed Fourier transform data; cf., e.g., [21].

Example 6.1. We illustrate our findings for a single point source

$$f \;=\; c\delta_z$$

with "strength" $c = 1 + \mathrm{i}$ located at $z = (8, 5)$. For this example we use the wave number $\kappa = 10$ and take $n = 256$ samples of the far field at an equidistant grid over S^1. A fast Fourier transform of the windowed data yields approximations of the windowed Fourier transform for frequencies $\omega \in [-127, 127]$ and, hence, approximations of $(R(g_\varepsilon * f))(\theta, s)$ for $s \in [-12.7, 12.7]$ according to (6.5). For the window we use a Gaussian χ_ε with standard deviation $\varepsilon = \pi/36$, but numerically we put the values of χ_ε to zero for $|t| > 3\varepsilon = \pi/12$. According to (4.3) this (essentially) corresponds to a Gaussian blur g_ε in the image domain with standard deviation

$$\frac{1}{\varepsilon\kappa} \;=\; \frac{3.6}{\pi}\,. \tag{6.6}$$

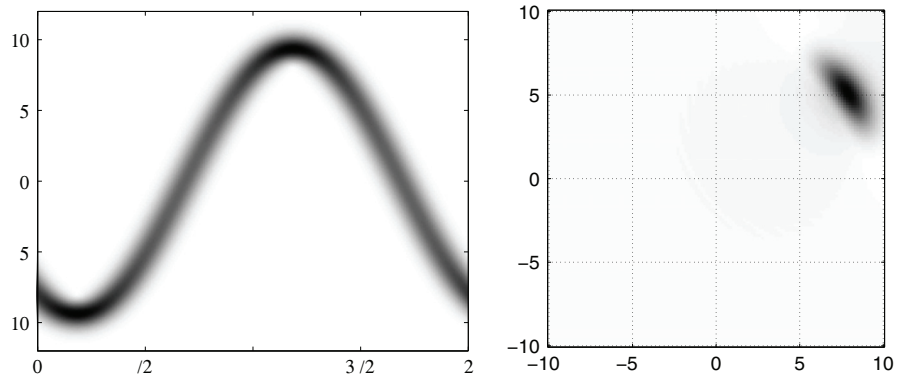

FIG. 6.2. *Same as Figure* 6.1*, but using a windowed Fourier transform with a window support which is twice as large* ($\varepsilon = \pi/18$).

In view of our discussion in Example 4.2, the width of this blur is $2/(\varepsilon\kappa) \approx 2.3$.

This is nicely confirmed in Figure 6.1 which shows the corresponding sinogram (6.5) as a gray-scale plot, where the polar angle ϑ of $\theta \in S^1$ varies along the horizontal axis and s along the vertical axis. The sine ribbon in this plot has a vertical diameter of about $2 \cdot 2/(\varepsilon\kappa) \approx 4.6$ as expected. The gray-scale plot on the right-hand side is the result of the filtered backprojection algorithm with these data, which looks like a Gaussian centered at the source z with width $2/(\varepsilon\kappa)$; cf. Figure 4.1.

In order to increase the resolution of the reconstruction it would be necessary to decrease $1/(\varepsilon\kappa)$, i.e., to increase ε. Figure 6.2 shows the corresponding result with ε increased by a factor of two. This figure exhibits several interesting features: First, it can indeed be seen that the sine ribbon is now narrower (although its width is not exactly half the former one); second, the intensity of the ribbon now varies with θ. This variation is due to the fact that the remainder term in Proposition 3.1 is no longer negligible. As a consequence, the filtered backprojection yields only a distorted two-dimensional Gaussian; cf. the corresponding right-hand plot. We note that for this source term and wave number the reconstruction in Figure 6.2 is about the best (i.e., the most localized) that we can get with this method. ◇

Example 6.2. For a second example we return to the (previous) smaller window size, i.e., $\varepsilon = \pi/36$, and add two further point sources at $z_2 = (-2, 2)$ and $z_3 = (4, -8)$ with "strengths" $c_2 = 2\mathrm{i}$ and $c_3 = 1$, using the same algorithm (and wave number) as before. Figure 6.3 shows the corresponding numerical results. Here and in all subsequent plots we enhance the "reconstruction" by a simple postprocessing: We subtract the mean of the result of the filtered backprojection in the region of interest $[-10, 10]^2$, and then reset all negative values to zero.

In this example—due to linearity—the windowed Fourier transform yields a superposition of three sine ribbons that correspond to the individual point sources. However, when we switch to the absolute values of the windowed Fourier transform in (6.5), this introduces artifacts into the resulting sinogram due to interferences of the sine ribbons where they cross each other. Still, the reconstruction by the filtered backprojection shows three approximate two-dimensional Gaussians centered at the correct source points. ◇

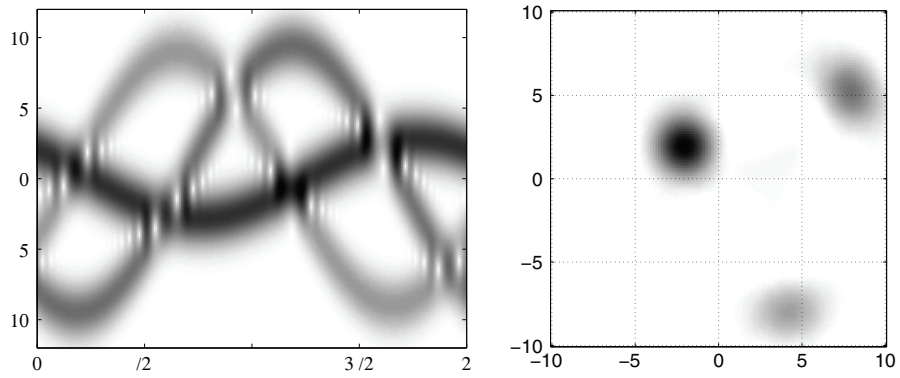

FIG. 6.3. *Same as Figure* 6.1*, but with three point sources and postprocessing (see text).*

7. Resolution and limitations. In order to discuss the resolution and the limitations of our method we need to determine the optimal window size ε for a given product κR, where $R > 0$ is such that $\operatorname{supp} f \subset B_R(0)$; note that the far field u^∞ depends only on the product of κ and R, but not on the individual factors independently. Therefore, without loss of generality we subsequently freeze the geometry of the scatterers and consider the resolution as a function of κ only.

To do so, let $\theta = (\cos\vartheta, \sin\vartheta)$ and $\widehat{x}_{\vartheta+t} = \big(\cos(\vartheta+t), \sin(\vartheta+t)\big)$, and consider the function

$$v_\theta(t) \,=\, \chi_\varepsilon(t) u^\infty(\widehat{x}_{\vartheta+t})\,, \qquad t \in \mathbb{R}\,,$$

which is to be Fourier transformed in (3.4). With N equidistant samples of the far field and a simple quadrature approximation we obtain

$$(S_\varepsilon u^\infty)(\theta,\omega) \,=\, \int_{-\infty}^{\infty} e^{-\mathrm{i}\omega t} v_\theta(t)\,\mathrm{d}t \,\approx\, \frac{2\pi}{N} \sum_{l=-\infty}^{\infty} e^{-\mathrm{i}\omega l 2\pi/N} v_\theta(l2\pi/N)\,,$$

the latter series being in practice a finite one, since—after cropping the window χ_ε at $\pm 3\varepsilon$—the function v_θ has compact support in $[-3\varepsilon, 3\varepsilon]$. It follows that, for $L \geq N$ even,

$$(S_\varepsilon u^\infty)(\theta,\omega_k) \,\approx\, \frac{2\pi}{N} \sum_{l=1-L/2}^{L/2} e^{-\mathrm{i}lk2\pi/L} v_\theta(l2\pi/N)\,, \qquad \omega_k = kN/L\,, \tag{7.1}$$

and, hence, $\big(S_\varepsilon u^\infty\big)(\theta,\,\cdot\,)$ can be approximated with a fast Fourier transform of the vector $\big[v_\theta(l2\pi/N)\big]_l$ for a grid of frequencies ω_k, $k = 1-L/2, \ldots, L/2$, that covers the interval $(-N/2, N/2)$ with mesh width

$$\Delta\omega \,=\, N/L \,\leq\, 1\,.$$

We can thus trigger L to achieve a suitable resolution in the frequency space.

By virtue of (6.5) the right-hand side of (7.1) provides an approximation of the Radon transform $\big(Rf\big)(\theta^\perp, s)$ for $s \in (-N/(2\kappa), N/(2\kappa))$. As the support of the Radon transform is constrained by $s \in [-R - 3/(\varepsilon\kappa), R + 3/(\varepsilon\kappa)]$ (cf. (6.6)), we require

$$N \,\geq\, 2\kappa(R + 3/(\varepsilon\kappa)) \tag{7.2}$$

for the sinogram to be complete. Note that the additional term $3/(\varepsilon\kappa)$ must not be neglected in (7.2); in the previous examples we have had $3/(\varepsilon\kappa) \approx R/4$.

The standard Fourier analysis for the Radon transform (cf. [21, sects. V.1 and III]) recommends that the number N of angular samples from S^1 should be greater than bR, provided that the function to be reconstructed is essentially bandlimited with bandwidth b while being supported in $|x| < R$ at the same time. In our case the function to be reconstructed is $g_\varepsilon * f^*$, the particular source f^* having been fixed in section 5, and the corresponding (essential) bandwidth of $g_\varepsilon * f^*$ has been determined in (5.4). This yields the lower bound $N \geq \kappa R\sqrt{1+9\varepsilon^2}$ for N, which is somewhat smaller than the bound in (7.2); in fact, in all our examples

$$N \geq 2.5\,\kappa R \tag{7.3}$$

has been a sufficient requirement to satisfy both bounds for N simultaneously, and this is what we recommend using.

At the same time the grid spacing $\Delta\omega$ of the other variable should satisfy the inequality (see [21])

$$\Delta\omega \lesssim \frac{\pi}{bR}\,\kappa R = \frac{\pi}{\sqrt{1+9\varepsilon^2}}\,.$$

As this recommendation is based on the assumption that b is "sufficiently large" (cf. [21, p. 111]), it is useful to reduce the size of $\Delta\omega$ when κR is only of the order of a few tens, or so, to increase the resolution of the sinogram (see Example 7.1 below). Recall that this can be achieved by choosing L sufficiently large in (7.1), independent of the given number of sampled far field data.

Now we turn to some numerical experiments to illustrate the resolution we can achieve with this approach, as well as its limitations.

Example 7.1. We reconsider Example 6.2 with the same three sources, but vary the wave number from $\kappa = 5$ to $\kappa = 10$ to $\kappa = 20$. For $\kappa = 20$ the $N = 256$ data points that we have used so far fail to satisfy the bound (7.3); hence for $\kappa = 20$ we use twice as many data. For all three wave numbers we have optimized the window size with respect to resolution, at the price of a certain distortion. For $\kappa = 10$, for example, we repeat the experiment of Example 6.2 with the larger window size $\varepsilon = \pi/18$; for $\kappa = 20$ we use $\varepsilon = \pi/24$, and $\varepsilon = \pi/5$ for $\kappa = 15$. It can be seen in Figure 7.1 that the sine ribbons vary in magnitude with respect to θ, showing that the approximation of the Radon transform is just at the edge of getting less accurate. Accordingly, the reconstructions are somewhat distorted. From these reconstructions we conclude that the radii of the bell-shaped approximations of the point sources decrease with increasing wave number.

In all three cases the particular source that is reconstructed best is the one closest to the origin. This is due to the fact that the radius of an individual source point enters via the factor $|z|$ in the error estimate (3.5); accordingly, the approximation of the two sine ribbons from the outer sources is inferior to the one for the source near the center. It is for this reason that the reconstructions of the outer two source points are even blurrier with respect to the angular variable.

Finally, we also show an analogous result for $\kappa = 2$. As can be seen from the corresponding sinogram in Figure 7.2, the sine ribbons do overlap severely for this small wave number, and hence the approximate Radon data suffer from strong interferences. Still, the reconstruction is reasonable. If κ is decreased somewhat further, say if $\kappa = 1$, then the method does deteriorate eventually. Note that for this example

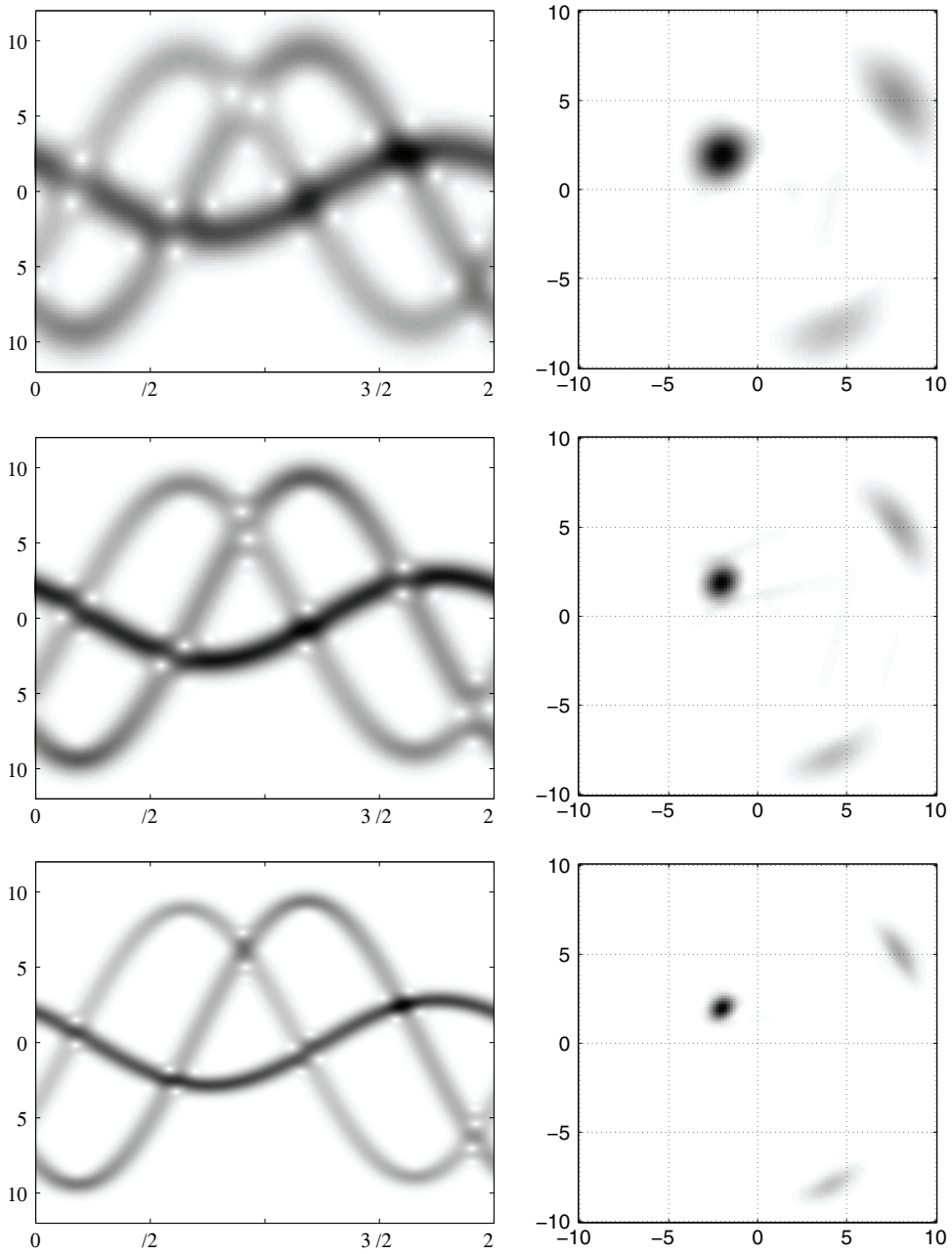

FIG. 7.1. *Same geometry as in Figure* 6.3*, but now with varying* κ *and* ε*. Top:* $\kappa = 5$*,* $\varepsilon = \pi/15$*. Middle:* $\kappa = 10$*,* $\varepsilon = \pi/18$*. Bottom:* $\kappa = 20$*,* $\varepsilon = \pi/24$*. Reconstructions have been postprocessed.*

we have chosen $L = 4N$ in (7.1), for otherwise the grid that is used for the variable σ would consist of only 24 grid points inside the portion of the sinogram that is shown in Figure 7.2. ◇

Based on these empirical results we include in Figure 7.3 a plot of $\varepsilon = \varepsilon(\kappa)$ (rescaled by $1/\pi$ to allow a better comparison with the numbers listed above) and the

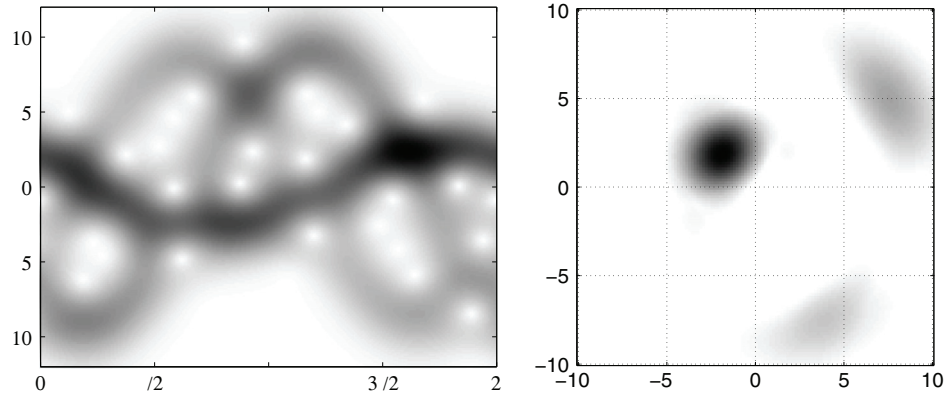

FIG. 7.2. *Same as Figure* 7.1*, but now with* $\kappa = 2$ *and optimal* $\varepsilon = \pi/9$*. Reconstruction has been postprocessed.*

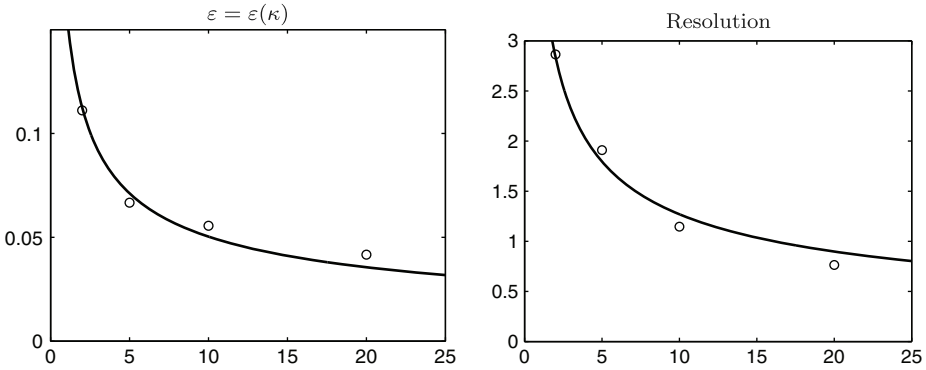

FIG. 7.3. *Plot of* ε/π *(left) and resolution* $r_2 = 2/(\varepsilon\kappa)$ *(right) versus wave number* κ*.*

corresponding resolution $r_2 = 2/(\varepsilon\kappa)$ (cf. (6.6)) as a function of the wave number κ; recall that r_2 is an estimate of the width of the blur that smears out a point source in the reconstruction. In these plots the circles correspond to the respective values of ε and r_2 that we have found to be optimal in Example 7.1. The solid lines show the graph of certain functions $\kappa \mapsto c/\sqrt{\kappa}$ for suitable constants c; this indicates that ε and r_2 decay antiproportionally with $\sqrt{\kappa}$.

Example 7.2. In an attempt to study the sensitivity of our algorithm with respect to noise in the data, we return once more to Example 6.2 with wave number $\kappa = 10$ and $\varepsilon = \pi/36$ but add 50% uniformly distributed relative error to the far field data before computing the windowed Fourier transform. More precisely, we generate vectors $e_1, e_2 \in \mathbb{R}^{256}$ containing pseudorandom numbers drawn from the standard uniform distribution on $(-0.5, 0.5)$ and add

$$0.5\|u^\infty\|_2 \frac{e_1 + \mathrm{i}e_2}{\|e_1 + \mathrm{i}e_2\|_2}$$

to the far field data u^∞. Figure 7.4 shows the corresponding numerical results. Although the sinogram is significantly distorted, the quality of the reconstruction is still acceptable (cf. Figure 6.3); the noise manifests itself only by some faint oscillations in between the scatterers. Numerical tests confirm that choosing a larger window size,

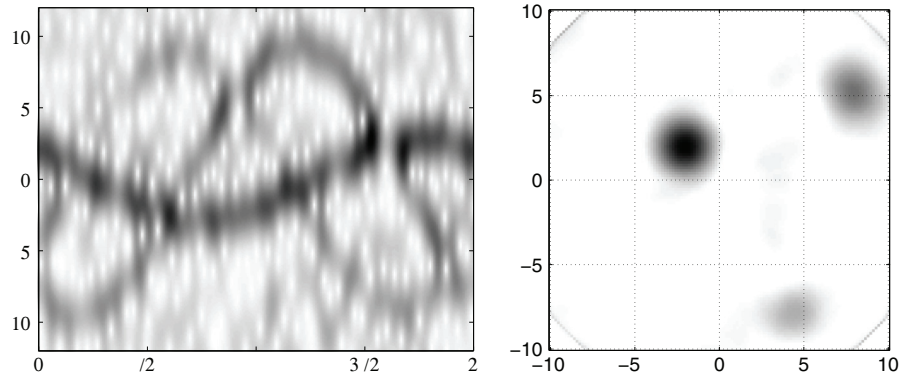

FIG. 7.4. *Same as Figure* 6.3*, but using data containing* 50% *uniformly distributed noise;* $\varepsilon = \pi/36$*. Reconstruction has been postprocessed.*

i.e., less smoothing and better resolution (cf. Example 7.1), yields stronger oscillations and inferior reconstructions. Note that the circular artifact near the boundary of the picture comes from the fact that the noise is restricted to the data that are given on the interval $[0, 2\pi] \times [-12.7, 12.7]$ of the windowed Fourier transform domain, and data beyond that interval are taken to be zero. In the reconstruction this in turn corresponds to some virtual object (or singularity) supported on a disk with radius 12.7 . ◇

8. Possible extensions. We discuss two possible extensions of the algorithm presented so far. The first concerns limited angle problems, while the second deals with inverse obstacle scattering problems.

8.1. Limited data problems. Before we start we note that the Radon transform data satisfy

$$\big(Rf\big)(\theta, s) \;=\; \big(Rf\big)(-\theta, -s) \qquad \text{for all } \theta \in S^1 \text{ and } s \in \mathbb{R}\,, \tag{8.1}$$

and hence, when θ runs through the entire sphere S^1, half of the Radon data are redundant. However, for the right-hand side of (6.5), i.e., the approximate Radon data given by the absolute values of the windowed Fourier transform, this identity fails to be true in general, although it does hold for real source terms f, or for single point sources. We can take advantage of this failure by averaging the corresponding approximations for the two terms in (8.1) before calling the filtered backprojection algorithm. On the other hand, the impact on the numerical results appears to be marginal.

Turning to limited data problems, it is well known that the Radon transform can still be inverted if data are only given for less than half the sphere S^1, say when the polar angle ϑ of $\theta \in S^1$ is confined to some interval $\vartheta \in [0, \beta]$ with $\beta < \pi$ (cf., e.g., [21]). However, limited data problems are notoriously ill-posed. In our approach, if the far field u^∞ of (2.3) is given only for $\vartheta \in [0, \beta]$ with $\beta < \pi$, then we can still compute its windowed Fourier transform for all angles $\vartheta \in [3\varepsilon, \beta - 3\varepsilon]$, where as before, ε is the standard deviation of the Gaussian window. We can then use any sophisticated algorithm for inverting the limited angle Radon transform (cf., e.g., [21, sect. VI.2]) to approximate the source f, or rather its mollification $g_\varepsilon * f$.

Here we present a numerical result for a very ad hoc modification of our previous algorithm: We simply set all unknown far field samples to zero and treat this

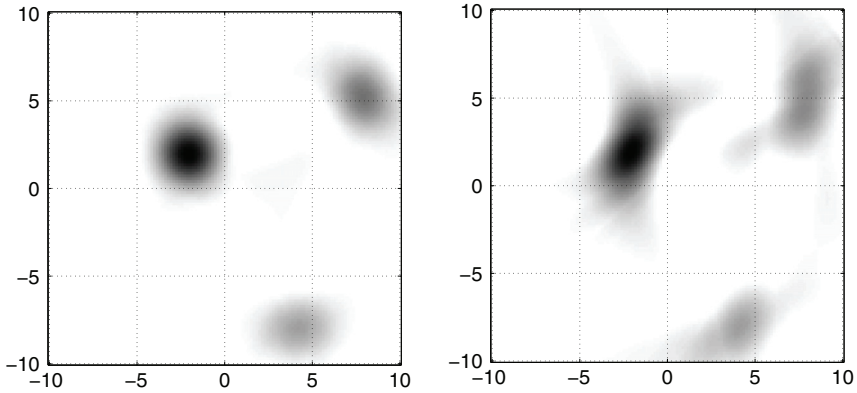

FIG. 8.1. *Reconstruction of three point sources with $\kappa = 10$ and $\varepsilon = \pi/36$. Left: full data. Right: limited angle data, $\vartheta \in (0, 2\pi/3)$. Both reconstructions have been postprocessed.*

augmented data as full-view input to our scheme. Figure 8.1 shows the corresponding reconstruction for the setting from Example 6.2, but now given only data $u^\infty(\theta)$ for $\vartheta \in [0, 2\pi/3]$, i.e., significantly less than a half-circle. The radius of the window that has been used is $\varepsilon = \pi/36$ as in Example 6.2. Qualitatively, the result is not much worse than the corresponding one for full data, although the limited angle reconstruction is clearly distorted.

8.2. Inverse obstacle scattering. In inverse obstacle scattering the measured data is the far field corresponding to a solution u of the homogeneous Helmholtz equation in the exterior of an unknown obstacle $\Omega \subset \mathbb{R}^2$, with known or unknown boundary condition on $\partial\Omega$. Under mild assumptions the solution u can be written as a single layer potential over the boundary of Ω; i.e., u is the solution of a source problem (2.1) with the source term f supported on the boundary of the obstacle.

Apparently, such a source can be interpreted as a superposition of infinitely many point sources (a continuum), so that interference of the corresponding sine ribbons occurs everywhere, not only at exceptional angles. Still, decent reconstructions are obtained with the very same algorithm as before, that is, with the filtered backprojection applied to the absolute values of the windowed Fourier transform as approximate Radon data.

Figure 8.2 shows numerical results for a test case with two scattering obstacles illuminated by an incoming plane wave from the left. These two obstacles have different physical properties: The kite in the upper right corner of the region of interest is implemented to be sound-hard, whereas the ellipse is taken to be sound-soft. Accordingly, the scattered field satisfies a Neumann condition on the kite's boundary and a Dirichlet condition on the boundary of the ellipse. For this example we use the same wave number $\kappa = 10$ and the same window radius $\varepsilon = \pi/36$ as in Example 6.2; however, in order to comply with the constraint (7.3) and the somewhat larger value of R we now use $N = 280$ far field samples. For a proper physical evaluation of this result we remark that $\kappa = 10$ corresponds to a wave length of $\lambda \approx 0.63$ units; this means that the smaller diameter of the ellipse equals about 3.5λ.

Note that the reconstruction in Figure 8.2 not only gives an upper bound for the convex source support $\mathscr{C}$ of the far field of the scattered wave (see section 5) but actually contains even more qualitative information on the location of possible sources within $\mathscr{C}$.

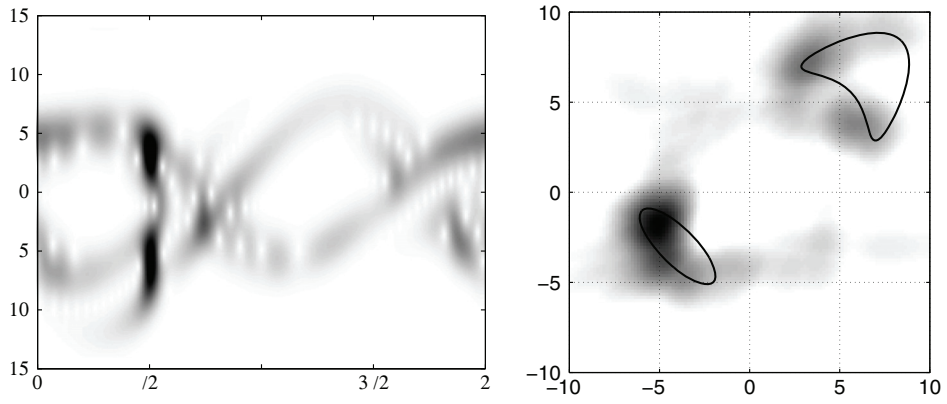

FIG. 8.2. *Left: approximation of the exponential Radon transform for inverse obstacle scattering. Right: reconstruction with filtered backprojection and postprocessing.*

9. Summary. We have considered the inhomogeneous two-dimensional Helmholtz equation, where the inhomogeneity is given by a source supported on a compact set. For the radiating solution of this source problem, we have established that—under certain assumptions—the windowed Fourier transform (with Gaussian filter, for example) of the corresponding far field can be considered as an approximation of the exponential Radon transform of the source, and, up to some unavoidable interferences, the absolute values of these data approximate classical Radon transform data for the parallel scanning geometry in the plane.

We have observed numerically that the resolution of the reconstructed images improves with the square root of the wave number κ if the standard deviation of the Gaussian window decreases like $1/\sqrt{\kappa}$. A critical parameter of the method is the product κR, where R is the radius of the smallest circle around the origin that encloses the support of the source, because twice this number is a rough estimate of the minimal number N of far field samples that are required as input data; cf. (7.3). It turns out that the method performs best when κR is of the order of 100, in which case about $N = 256$ equidistant samples of the far field are required.

REFERENCES

[1] C. ALVES, R. KRESS, AND P. SERRANHO, *Iterative and range test methods for an inverse source problem for acoustic waves*, Inverse Problems, 25 (2009), 055005.

[2] O. M. BUCCI, A. CAPOZZOLI, AND G. D'ELIA, *Determination of the convex hull of radiating or scattering systems: A new, simple and effective approach*, Inverse Problems, 18 (2002), pp. 1621–1638.

[3] O. M. BUCCI, A. CAPOZZOLI, G. D'ELIA, AND M. SANTOJANNI, *Scatterers localization in the circular scanning geometry*, in Proceedings of the 2004 URSI-EMTS International Symposium on Electromagnetic Theory, Pisa, Italy, 2004, pp. 903–905.

[4] D. COLTON AND R. KRESS, *Inverse Acoustic and Electromagnetic Scattering Theory*, 2nd ed., Springer, Berlin, 1998.

[5] R. DAUTRAY AND J.-L. LIONS, Mathematical Analysis and Numerical Methods for Science and Technology, Vol. 1, Springer, Berlin, 1990.

[6] A. J. DEVANEY, *A filtered backpropagation algorithm for diffraction tomography*, Ultrason. Imaging, 4 (1982), pp. 336–350.

[7] A. J. DEVANEY, *Reconstructive tomography with diffracting wavefields*, Inverse Problems, 2 (1986), pp. 161–183.

[8] A. J. Devaney, E. A. Marengo, and M. Li, *Inverse source problem in nonhomogeneous background media*, SIAM J. Appl. Math., 67 (2007), pp. 1353–1378.
[9] A. El Badia and T. Nara, *An inverse source problem for Helmholtz's equation from the Cauchy data with a single wave number*, Inverse Problems, 27 (2011), 105001.
[10] M. Eller and N. P. Valdivia, *Acoustic source identification using multiple frequency information*, Inverse Problems, 25 (2009), 115005.
[11] A. C. Fannjiang, T. Strohmer, and P. Yan, *Compressed remote sensing of sparse objects*, SIAM J. Imaging Sci., 3 (2010), pp. 595–618.
[12] R. Griesmaier, *Multi-frequency orthogonality sampling for inverse obstacle scattering problems*, Inverse Problems, 27 (2011), 085005.
[13] M. Hanke, *One shot inverse scattering via rational approximation*, SIAM J. Imaging Sci., 5 (2012), pp. 465–482.
[14] S. Helgason, *The Radon Transform*, Birkhäuser Boston, Boston, 1980.
[15] A. Hertle, *On the injectivity of the attenuated Radon transform*, Proc. Amer. Math. Soc., 92 (1984), pp. 201–205.
[16] L. Hörmander, *The Analysis of Linear Partial Differential Operators.* I. *Distribution Theory and Fourier Analysis*, Springer-Verlag, Berlin, 1983.
[17] M. Ikehata, *Reconstruction of a source domain from the Cauchy data*, Inverse Problems, 15 (1999), pp. 637–645.
[18] V. Isakov, *Inverse Source Problems*, AMS, Providence, RI, 1990.
[19] S. Kusiak and J. Sylvester, *The scattering support*, Comm. Pure Appl. Math., 56 (2003), pp. 1525–1548.
[20] S. Kusiak and J. Sylvester, *The convex scattering support in a background medium*, SIAM J. Math Anal., 36 (2005), pp. 1142–1158.
[21] F. Natterer, *The Mathematics of Computerized Tomography*, Teubner, Stuttgart, John Wiley & Sons, Chichester, UK, 1986.
[22] F. Natterer, *The Attenuated Radon Transform for Complex Attenuation*, manuscript, 2007; available from www.math.uni-muenster.de/num/Preprints.
[23] F. Natterer, *Inversion of the Fourier Transform without Low Frequencies*, manuscript, 2007; available from www.math.uni-muenster.de/num/Preprints.
[24] R. Potthast, *A study on orthogonality sampling*, Inverse Problems, 26 (2010), 074015.
[25] W. Rudin, *Real and Complex Analysis*, McGraw-Hill, New York, 1966.
[26] R. S. Strichartz, *Radon inversion—variations on a theme*, Amer. Math. Monthly, 89 (1982), pp. 377–384, 420–423.
[27] J. Sylvester, *Notions of support for far fields*, Inverse Problems, 22 (2006), pp. 1273–1288.
[28] O. Tretiak and C. Metz, *The exponential Radon transform*, SIAM J. Appl. Math., 39 (1980), pp. 341–354.
[29] J. You, *The attenuated Radon transform with complex coefficients*, Inverse Problems, 23 (2007), pp. 1963–1971.